Icarus 254 (2015) 306–323

Contents lists available at ScienceDirect

Icarus

journal homepage: www.elsevier.com/locate/icarus

General circulation models of the dynamics of Pluto's volatile transport on the eve of the *New Horizons* encounter

Anthony D. Toigo [a,*], Richard G. French [b], Peter J. Gierasch [c], Scott D. Guzewich [d], Xun Zhu [a], Mark I. Richardson [e]

[a] Johns Hopkins University Applied Physics Laboratory, Laurel, MD 20723, United States
[b] Wellesley College, Wellesley, MA 02492, United States
[c] Astronomy Department, Cornell University, Ithaca, NY 14853, United States
[d] NASA Goddard Space Flight Center, Greenbelt, MD 20771, United States
[e] Ashima Research, Pasadena, CA 91106, United States

ARTICLE INFO

Article history:
Received 19 December 2014
Revised 6 March 2015
Accepted 31 March 2015
Available online 6 April 2015

Keywords:
Pluto
Pluto, atmosphere
Atmospheres, dynamics

ABSTRACT

Pluto's atmospheric dynamics occupy an interesting regime in which the radiative time constant is quite long, the combined effects of high obliquity and a highly eccentric orbit can produce strong seasonal variations in atmospheric pressure, and the strong coupling between the atmosphere and volatile transport on the surface results in atmospheric flows that are quite sensitive to surface and subsurface properties that at present are poorly constrained by direct observations. In anticipation of the *New Horizons* encounter with the Pluto system in July 2015, we present a Pluto-specific three-dimensional general circulation model (GCM), PlutoWRF, incorporating the most accurate current radiative transfer models of Pluto's atmosphere, a physically robust treatment of nitrogen volatile transport, and the flexibility to accommodate richly detailed information about the surface and subsurface conditions as new data become available. We solve for a physically self-consistent, equilibrated combination of surface, subsurface, and atmospheric conditions to specify the boundary conditions and initial state values for each GCM run. This is accomplished using two reduced versions of PlutoWRF: a two-dimensional surface volatile exchange model to specify the properties of surface nitrogen ice and the initial atmospheric surface pressure, and a one-dimensional radiative–conductive–convective model that uses the two-dimensional model predictions to determine the corresponding global-mean atmospheric thermal profile. We illustrate the capabilities of PlutoWRF in predicting Pluto's general circulation, thermal state, and volatile transport of nitrogen by calculating the dynamical response of Pluto's atmosphere, based on four different idealized models of Pluto's surface ice distribution from Young (Young, L.A. [2013]. Astrophys. J. 766, L22) and Hansen et al. (Hansen, C.J., Paige, D.A., Young, L.A. [2015]. Icarus 246, 183). Our GCM runs typically span 30 years, from 1985 to 2015, covering the period from the discovery of Pluto's atmosphere to present. For most periods simulated, zonal winds are strongly forced by a gradient wind balance, relaxing in later (recent) years to an angular momentum conservation balance of the seasonal polar cap sublimation flow. Near-surface winds generally follow a sublimation flow from the sunlit polar cap to the polar night cap, with a Coriolis turning of the wind as the air travels from pole to pole. We demonstrate the strong contribution of nitrogen sublimation and deposition to Pluto's atmospheric circulation. As *New Horizons* data become available, PlutoWRF can be used to construct models of Pluto's atmospheric dynamics and surface wind regimes more constrained by physical observations.

1. Introduction

Since the discovery of Pluto's atmosphere more then 25 years ago (Hubbard et al., 1988; Elliot et al., 1989; Brosch, 1995), extensive observations and theoretical analysis have revealed a great deal about the composition, thermal structure, and surface interactions of this tiny icy world's cold and tenuous nitrogen-rich atmosphere. We know that the radiative time constant of the upper atmosphere is quite long, up to several years (Strobel et al., 1996), and the atmosphere appears to be in vapor pressure equilibrium with the surface (Owen et al., 1993). Our most detailed

* Corresponding author.
E-mail address: Anthony.Toigo@jhuapl.edu (A.D. Toigo).

http://dx.doi.org/10.1016/j.icarus.2015.03.034
0019-1035/

knowledge of the thermal structure of Pluto's atmosphere comes from an abundant set of stellar occultation observations, made possible by Pluto's fortuitous ongoing passage across the dense star fields of the Milky Way as seen from the Earth. Occultations (e.g., Elliot and Young, 1992; Elliot et al., 2003, 2007; Young et al., 2008; Zalucha et al., 2011a,b) have shown that Pluto's atmosphere, above the lowest few scale heights, is nearly isothermal, with a temperature of about 100 K (with deviations less than about 5 K) to the upper extent of retrievals. The surface temperature is only about 40 K, and thus the lower atmosphere must include a strongly stratified thermal inversion. This marks a new, scientifically interesting dynamical regime for planetary atmospheres that is not yet well understood.

As on Mars (and unlike Earth and Venus, for example), Pluto's dominant atmospheric constituent, N_2, freezes and sublimes, likely resulting in winds and changes in the surface pressure and atmospheric thermal state on seasonal and diurnal timescales. Volatile transport models predict a wide range of variations in frost distribution and atmospheric pressure over the course of Pluto's 248-year highly eccentric orbit (Hansen and Paige, 1996; Young, 2012, 2013; Hansen et al., 2015), strongly dependent on the assumed but observationally uncertain surface conditions such as total volatile inventory, thermal inertial of the surface and subsurface, and emissivity, spatial distribution, and albedo of surface ice.

Although variations in the observationally inferred surface atmospheric pressure from 1988 to the present should in principle provide strong constraints on Pluto's average surface volatile distribution over its orbital period, evidence from recent stellar occultations has led to disagreement over whether Pluto retains its atmosphere during all seasons (Olkin et al., 2015; Bosh et al., 2015) or whether there may be a total collapse of the atmosphere in the near future (Person, 2013). Thus, we cannot confidently exclude the possibility that, unlike Mars, almost the entirety of Pluto's atmosphere may freeze onto the surface for a significant portion of its orbit. Additional observations will help limit the suite of possibilities, of course, but only with modeling tools such as a general circulation model (GCM) can we investigate the likely changes in atmospheric structure, surface pressure, surface winds, and global atmospheric dynamics over a full Pluto year.

With the imminent encounter of *New Horizons* with the Pluto system, many of the currently poorly known physical and thermal properties of the surface and subsurface may soon be more tightly constrained. Among these are the distribution, composition, and durability of surface volatiles, the nature and extent of a possible troposphere, the properties of atmospheric thermal tides and waves, the presence of clouds or hazes, and the rate of atmospheric escape. Additionally, visible evidence on Pluto's surface of atmospheric dynamical processes, such as wind-blown streaks, aeolian features, geysers, or even dune fields may well be detectable in *New Horizon's* high-resolution images. On the eve of this new era in planetary exploration, this is an opportune time to contextualize Pluto's atmosphere as a dynamically active climate system relative to other planets.

Our ultimate goal is to explore the dynamical changes in Pluto's atmosphere on diurnal to seasonal timescales, observationally motivated by a rich set of *New Horizons* and stellar occultation observations and investigated theoretically using a mature and extensively tested set of modeling tools. In this paper, we take a step in this direction by introducing the PlutoWRF GCM, a Pluto-specific variation of the generic planetWRF modeling system (Richardson et al., 2007). The model can be applied to a wide range of questions concerning Pluto's atmosphere, such as the strength and direction of both upper atmospheric and surface winds, the role of surface volatile sublimation and deposition (and its diurnal and seasonal variation) in controlling the atmospheric pressure and dynamical state, the nature and origin of atmospheric waves, and the presence and concentration of hazes and clouds. To help specify physically self-consistent initial conditions for the computationally intensive three-dimensional GCM runs, and to provide insight into the results of those simulations, we have developed two ancillary versions of PlutoWRF: a two-dimensional model for N_2 surface volatile transport, and a one-dimensional model of the globally-averaged atmospheric thermal state. With these tools in hand, we present GCM calculations of the dynamics and thermal structure of Pluto's atmosphere based on several idealized models of Pluto's volatile transport (Young, 2013; Hansen et al., 2015), over a decade timescale. These results will demonstrate the importance of volatile sublimation and deposition as a driver for large-scale dynamical activity, and they clarify some of the key physical processes that control both regional and seasonal atmospheric circulation and surface interactions.

We begin in Section 2 with a description of the PlutoWRF modeling framework, including the Pluto-specific changes we introduced to the generalized planetWRF model. In Section 3 we describe our two-dimensional surface volatile exchange model and compare it with similar models, and in Section 4 we develop the one-dimensional radiative–conductive–convective model implementation and indicate how it can be used to define the initial state for our full three-dimensional GCM runs. In Section 5 we apply this unified modeling framework to explore the predicted atmospheric dynamics associated with recent published models of volatile transport on Pluto's surface. Finally, in Section 6 we summarize our results and offers suggestions for future work.

2. Model description

PlutoWRF is the Pluto-specific implementation of the planetWRF model (Richardson et al., 2007), which itself is an expansion and extension of the National Center for Atmospheric Research (NCAR) Weather Research and Forecasting (WRF) model (Skamarock et al., 2008). WRF's modern design and capabilities have allowed it to be expanded to be applicable over a large range of study, from microscale processes to its use as a global model, as well as including three-dimensional data assimilation, several dynamical cores, and the ability to be run on massively parallel computing architectures. The WRF GCM integrates the fully compressible equations of fluid motion within a discrete ("grid-point") three-dimensional mesh. Orbital, physical, and atmospheric constants appropriate to each planet are defined, and explicitly simulated dynamical processes in the model are augmented by parameterization of unresolved processes, such as sub-grid-scale diffusion, boundary layer eddies and convection, radiative transfer, and phase-change processes (including the volatile cycle) and surface and subsurface heat exchange. The Pluto version of the model follows the IAU system for definition of the north pole (Zangari, 2015).

The multi-layer regolith heat exchange parameterization captures the diurnal, seasonal, and annual thermal waves, and is the same implementation as PlutoWRF's sister model MarsWRF (Toigo et al., 2012), with only the number of levels and surface constants (e.g., albedo and thermal inertia; also see Section 3) changed. The heat exchange is modeled as a diffusive process and the partial differential equation governing the change in regolith temperature with time is numerically implemented in an unconditionally stable Crank–Nicholson scheme. The regolith heat exchange parameterization is also linked to phase change parameterizations. For Pluto, only the N_2 cycle is currently implemented, although we plan to include other volatiles such as CO, CH_4, and even C_2H_6, which has recently been shown to be longitudinally variable on Pluto's surface (Holler et al., 2014). Surface ice cover is tracked through latent heat exchange in the atmosphere (by formation

and precipitation of N_2 ice aerosols if indicated) and on the surface (deposition and sublimation of surface ice).

The turbulence parameterization is the same as that used in the other planetary implementations of the planetWRF model, and is separated into horizontal and vertical components. In the horizontal, a two-dimensional version of the first-order Smagorinsky deformation scheme (Smagorinsky, 1963) is employed. In the vertical, boundary layer and free atmosphere turbulence is a modeled as a diffusive process (Hong et al., 2006).

Molecular diffusion is an important mixing process in Pluto's cold and thin atmosphere, and is included in PlutoWRF. The molecular diffusivity at each grid point and level is calculated based on a mean atmospheric molecular mass and local thermodynamic conditions (temperature, pressure, etc.), and an additional forcing term for relevant state variables (temperature, momentum, aerosols, and minor species mixing ratio) is then applied.

2.1. Radiative transfer parameterization

One of the most fundamental defining additions to PlutoWRF is the incorporation of an accurate and realistic radiation parameterization scheme to describe the heating and cooling of Pluto's atmosphere and surface. PlutoWRF includes multiple schemes, ranging from a simple Newtonian relaxation scheme (trending towards an equilibrium temperature profile) to a multi-species and multi-band model.

Radiative time constants in Pluto's atmosphere are quite long (Strobel et al., 1996), leading to small equator-to-pole temperature differences (see also Section 5). Nevertheless, a typical Pluto model simulation spans a sufficiently long time that an assumed equilibrium thermal profile would noticeably change over the course of the simulation. Therefore, we restrict our use of the Newtonian scheme to very short or idealized simulations with appropriate initial conditions. Instead, for all of the simulations described in this work, we use a multi-species multi-band parameterization of radiative heating due to CH_4 and CO gases as implemented in the scheme of Zhu et al. (2014). We exclude the escape processes in Pluto's upper atmosphere present in the one-dimensional model of Zhu et al. (2014) because the model top of PlutoWRF (up to order 10^3 km altitude) is typically much lower than the regions where atmospheric escape would be significant.

As a test of our implementation of the Zhu et al. (2014) model, Fig. 1 shows the heating and cooling rates of this radiative transfer scheme as calculated by the PlutoWRF implementation in a three-dimensional GCM simulation from the same seasonal period as Zhu et al. (2014), in a form for direct comparison with Fig. 5a of Zhu et al. (2014). Environmental inputs are the same (surface pressure, minor species mixing ratio, background thermal profile), but the vertical level structure (and spacing) are different for the two models. In general, the agreement in heating and cooling rates between the two models is very good, with some small differences in the altitude and magnitude of peak values. The most significant differences are in the diffusive heating rates, which are calculated in PlutoWRF using a turbulent and molecular diffusion scheme quite different from the Zhu et al. (2014) approach. The lower region of diffusive heating (between 300 and 550 km in altitude) is similar in vertical extent to the Zhu et al. (2014) result, but somewhat stronger in PlutoWRF, while the upper region (above 750 km) is stronger overall in the PlutoWRF calculation.

2.2. Initial and boundary conditions

As is the case for all other GCMs, PlutoWRF requires a set of initial and boundary conditions prior to the integration of the three-dimensional dynamical atmospheric model. These are specified either as a gridded set of global observations appropriate to the season of interest, or determined from values at the end of a spin-up period after which the model has reached some sort of quasi-equilibrium based on known inputs. As long as the spin-up period is sufficiently long to allow relaxation to a climatological mean state, the results should be insensitive to the exact choice of initial conditions.

For Pluto, the situation is complicated for both choices. Occultation observations of the atmospheric structure, while extremely useful, are sporadic and limited in temporal and spatial coverage, and prevent us from being able to start the model at any arbitrary point in time. They also derive atmospheric information only for temperature and pressure, with no information about winds. The relatively long length of Pluto's year, and the present uncertainty about Pluto's basic surface properties (e.g., thermal inertia and albedo), make long spin-up simulations impractical both with respect to computation resources and to realism of results.

Among the most important boundary conditions are the surface and subsurface properties that control heat flux and volatile abundance, such as regional variations of surface albedo, thermal inertia, ice composition and depth, and temperature. GCM results are highly sensitive to the specification of these properties since, for example, small changes in surface temperature will map to differences in surface ice coverage, which in turn map to changes in albedo (ice vs. rock) and surface pressure. Even in the absence of detailed observations of the actual conditions on Pluto, it is important to provide GCMs with physically self-consistent quasi-equilibrium values of the surface properties in order to obtain correspondingly self-consistent atmospheric and surface models without resorting to extremely long spin-up times.

Fortunately, specifying initial conditions for winds is a relatively less sensitive situation, because the relevant timescale for atmospheric momentum spin-up is far shorter than the seasonal timescale. We confirmed the insensitivity of the final wind state to the initial conditions from experiments in which we compared the results of three nearly identical GCM simulations, varying only the initial winds to be (1) at rest, (2) of the magnitude and direction of the values at the end of the previous simulation started from rest, and (3) in the opposite direction (but the same magnitude) of the values at the end of the first simulation started from rest. In all cases, the GCM simulations quickly achieved the same final wind state, independent of the initial conditions. Based on these results, we start our atmosphere initially at rest in all of our GCM simulations discussed below.

Occultation observations provide a convenient means of specifying Pluto's initial atmospheric thermal profile for a GCM run, but some uncertainty still exists, particularly regarding conditions nearest the surface. Because of the very strong positive atmospheric temperature gradient near the surface, differential refraction of the starlight deep in Earth-based stellar occultations prevents the determination of the surface pressure. In any event, occultation data are available for only a small fraction of Pluto's year, and an alternative method is needed to provide a realistic surface pressure for a given set of physical surface conditions.

In light of these requirements and restrictions, we have created two simpler implementations of PlutoWRF to provide self-consistent initial conditions for the much more computationally intensive three-dimensional GCM runs, and to provide insight into the results of those simulations. These two ancillary versions of PlutoWRF, a two-dimensional surface volatile exchange model and a one-dimensional radiative–conductive–convective model, both share the same infrastructure as the three-dimensional GCM version of PlutoWRF, and differ only in the specification of the model grid and the use (or lack thereof) of various physical parameterizations. We describe these models below, in the order

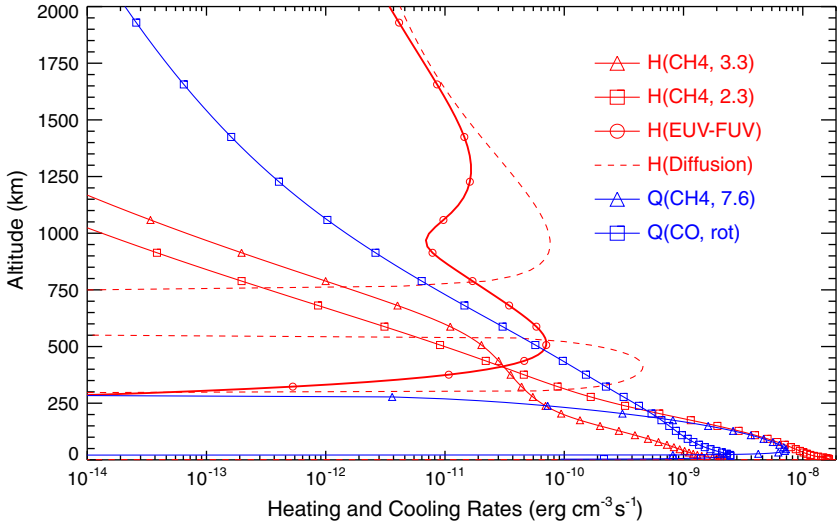

Fig. 1. Global-average (area-weighted) heating and cooling rate vertical profiles using the Zhu et al. (2014) radiative scheme as implemented in PlutoWRF from a GCM simulation at the same season and using the same inputs as those of Zhu et al. (2014). Units, symbols, colors, and notation are the same as those used in Zhu et al. (2014) for easy comparison with Fig. 5a therein. Heating rates are shown as red lines: H(CH4 3.3) and H(CH4 2.3) are the non-local-thermodynamic-equilibrium (LTE) heating rates by solar near-IR absorption in CH_4 3.3 and 2.3 μm vibrational bands, respectively; H(EUV–FUV) is the upper atmospheric heating rate due to solar FUV–EUV energy; H(diffusion) is the heating rate due to vertical turbulent diffusivity. Cooling rates are shown as blue lines: Q(CH4 7.6) is the non-LTE cooling rate due to the CH_4 7.6 μm vibrational band, and Q(CO, rot) is the LTE cooling rate by CO rotational lines. (For interpretation of the references to colour in this figure legend, the reader is referred to the web version of this article.)

that they are used to provide initial and boundary conditions on the three-dimensional GCM model.

3. 2D surface volatile exchange model

The two-dimensional surface volatile exchange version of PlutoWRF was designed to allow for multi-annual simulations that could make predictions of surface and subsurface temperature, surface ice coverage, and total atmospheric mass (or, equivalently, surface pressure). In this respect it is similar to other published surface volatile exchange models with the same goals and approaches (Hansen and Paige, 1996; Young, 2013; Hansen et al., 2015). However, our primary goal in constructing this reduced version of PlutoWRF was to provide self-consistent lower boundary conditions from multi-annual equilibrated simulations for use in three-dimensional GCM simulations.

Our two-dimensional volatile exchange model requires only a few parameterizations (see Section 2): surface and subsurface heat exchange, atmospheric and surface phase change, and surface radiation. The atmosphere as a whole is not explicitly modeled, but rather is parameterized as well and total atmospheric mass (surface pressure) at each grid point is tracked. Thus, the majority of the radiation parameterization in the full three-dimensional model (see Section 2.1) to calculate atmospheric heating rates is not used, and only the broadband amount of radiation reaching the surface is calculated. Additionally, only diurnally-averaged insolation is applied at the surface. This simplification is consistent with that used in Young (2013), and is justified as we are not concerned in this case with processes on a diurnal (or shorter) timescale.

The surface grid point mapping is the same as in the three-dimensional GCM. However, since only diurnally-averaged insolation is being applied, there is no need for a full grid point mapping of all longitudes; instead, a single longitude is specified as a representation of the zonal average. This reduces the problem to a two-dimensional calculation (in latitude and subsurface depth), which is much more computationally efficient than the full three-dimensional model, enabling quite rapid multi-annual simulations of volatile exchange.

The gridding in subsurface depth is implemented in the same fashion as that described in Hansen and Paige (1996), with sixty subsurface levels with that grow gradually thicker with depth. The initial conditions are specified as in Young (2013), with a moderate amount of atmosphere initially present (2 Pa), surface temperature in vapor pressure equilibrium with that amount of atmosphere, and subsurface temperature uniformly equal to the solid surface temperature. The lower boundary condition is also the same as Hansen and Paige (1996) and Young (2013) with an assumed conductive internal thermal heat flux of 6×10^{-3} W m^{-2}.

To demonstrate the validity of our reduction of the full three-dimensional GCM to a two-dimensional surface volatile exchange model, we compare our results with two other similar published models. First, in Fig. 2, predictions of surface pressure (Fig. 2A), and ice coverage (Fig. 2B) from a simulation using the same input parameters as Run #22 of Hansen et al. (2015) are plotted as a function of time and latitude. Ice coverage is shown as gray when the amount of surface ice is greater than 0.1 kg m^{-2}, or a layer of ice approximately 0.1 mm thick. Results are shown for the final four Pluto years of a 20-year run. Visual examination of the full 20 years of the simulation (see below) confirms that the model has essentially achieved a repeatable annual equilibrium after only a few Pluto years (and less than a Pluto decade), and thus these results do not represent a transient effect. This figure can be compared with the lowest two panels of Fig. 3 of Hansen et al. (2015). The overall agreement is excellent, with a slightly lower prediction of surface pressure during the period centered around southern summer, and ice coverage that is slightly less extensive towards the equator at its greatest extent. These differences are relatively small and are most likely traceable to subtle differences in the adopted N_2 vapor pressure equilibrium equation, where at temperatures typical of Pluto's cold surface, small changes ($\lesssim$1 K) in the temperature of solid N_2 can lead to order-of-magnitude differences in equilibrium vapor pressure.

Second, in Fig. 3, we show the predictions of atmospheric pressure at the surface (dotted lines) and at a radial distance of

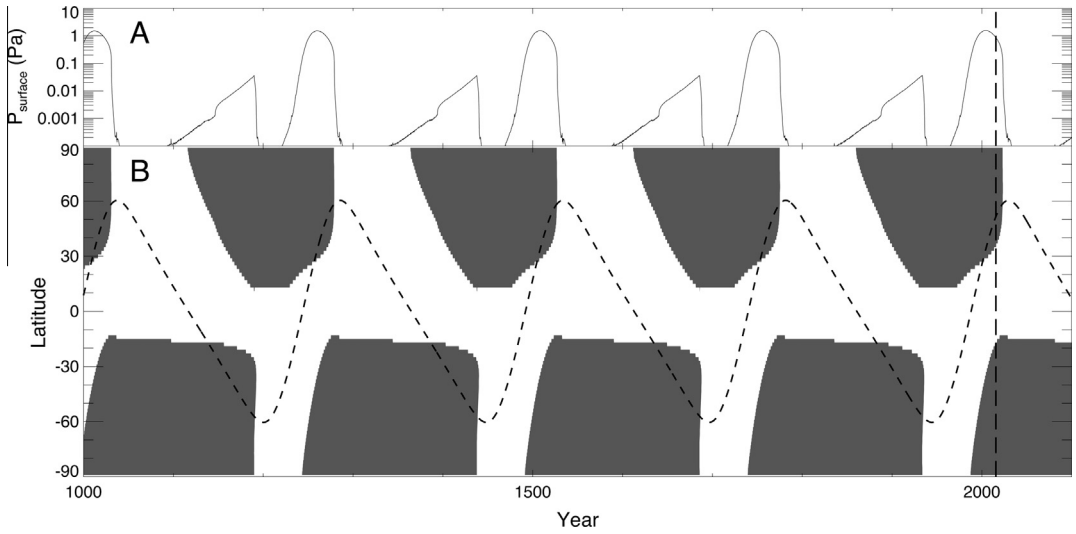

Fig. 2. Predictions of (A) surface pressure and (B) surface ice coverage (gray indicating presence of ice) as functions of time and latitude for a two-dimensional surface volatile exchange model simulation using the "best fit" run parameters (Run #22) from Hansen et al. (2015). The dotted line in (B) is the location of the subsolar latitude.

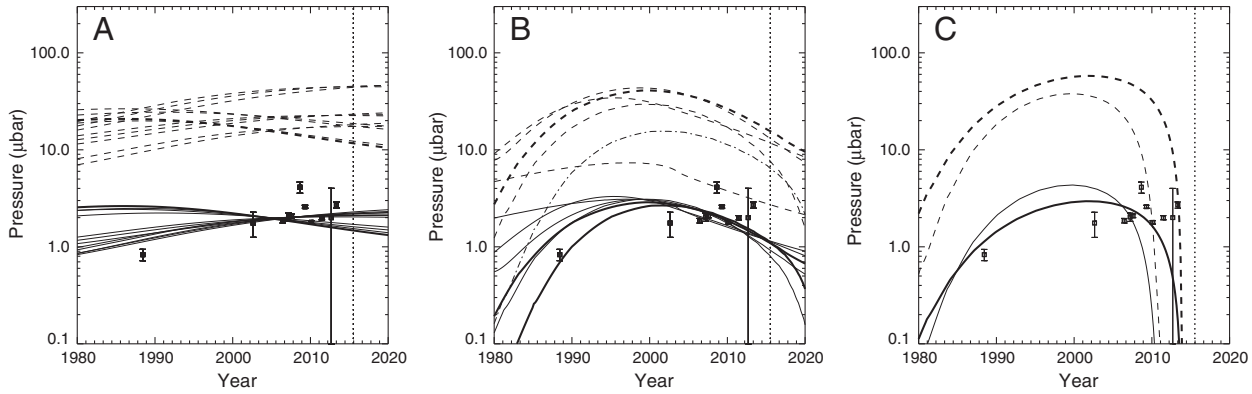

Fig. 3. Predictions of surface pressure (dotted lines) and pressure at 1275 km radial distance (solid lines) as a function of time for various surface conditions using the volatile transport heat balance model. Results are plotted as in Fig. 3 of Young (2013), with (A) showing the results from the PNV runs, (B) EPP runs, and (C) EEC runs. Included in (B) is the "best fit" run (Run #22) from Hansen et al. (2015) (with the dashed-dotted line representing surface pressure, and the dashed-triple-dotted line being pressure at 1275 km radial distance). Squares with error bars are measurements of pressure at a radial distance of 1275 km, as enumerated in Young (2013) with additional occultations as reported in Olkin et al. (2015).

1275 km (solid lines) for 1980–2020, based on a variety of simulations. The input parameters chosen are those of the 19 runs that were "qualitatively consistent with thermal, visible, and near-infrared data" from Table 1 of Young (2013), and Run #22 of Hansen et al. (2015). The categorization of simulations by similar seasonal trends in pressure (PNV: permanent northern volatile; EPP: exchange with pressure plateau; EEC: exchange with early collapse) are the same as those used in Young (2013), and this figure is directly comparable to Fig. 3 of that work. Our plotted results are taken from the final Pluto year of our 20-year simulations, substantially longer than the three year integrations used in Young (2013). (We use this longer integration period to ensure the achievement of quasi-equilibrium in our model.) Overall agreement is good here as well, with similar input parameters being categorized in the same seasonal trend groups (PNV, EPP, or EEC). Some of the PNV runs (Fig. 3A) show a somewhat earlier beginning to the predicted decrease in pressure, while some EPP runs show a somewhat slower and later decrease in pressure. The EEC runs also appear to show a slightly earlier collapse of the atmosphere, but compared to the length of a Pluto year, these differences are small. In particular, our EEC runs are consistent with those of Young (2013) in predicting that Pluto's atmosphere will have collapsed by the time of *New Horizons* closest approach to Pluto in July, 2015, for the assumed surface conditions.

Similar to the results of Young (2013), we found that one of the largest predictors of whether a given simulation will fall into the PNV, EPP, or EEC category was the value of the thermal inertia parameter. Low thermal inertias generally had large changes in surface pressure (EEC category), while high thermal inertias had more constant surface pressures (PNV category), and values in between having intermediate amplitude changes (EPP category). In order to test this hypothesis, we conducted a further series of simulations where all other parameters of the surface volatile exchange model were held constant (ice albedo, ice emissivity, and total volatile inventory) and only thermal inertia was varied. Two different test cases were chosen to provide the parameter values: the high thermal inertia run PNV9 of Young (2013) and the low thermal inertia Run #22 of Hansen et al. (2015). The results are shown in Figs. 4–6.

Fig. 4 shows the dependence on thermal inertia of the predicted seasonal changes in surface atmospheric pressure. The trends are similar for both test cases. For low thermal inertias (the solid line), seasonal changes in surface pressure are large (many orders of magnitude), as the bulk of the atmosphere essentially "freezes

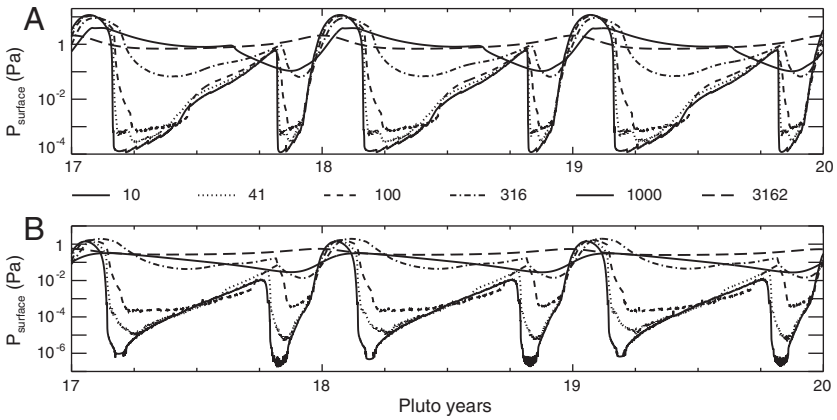

Fig. 4. Predictions of surface pressure showing the dependence on the surface thermal inertia. Six simulations are shown for each subfigure, with thermal inertia ranging from a value of 10 (solid line) to about 3000 (long-dashed line) in SI units. Output from the last three years of 20-year simulations are shown. (A) conditions equivalent to run PNV9 of Young (2013); (B) conditions equivalent to the "best fit" run from Hansen et al. (2015).

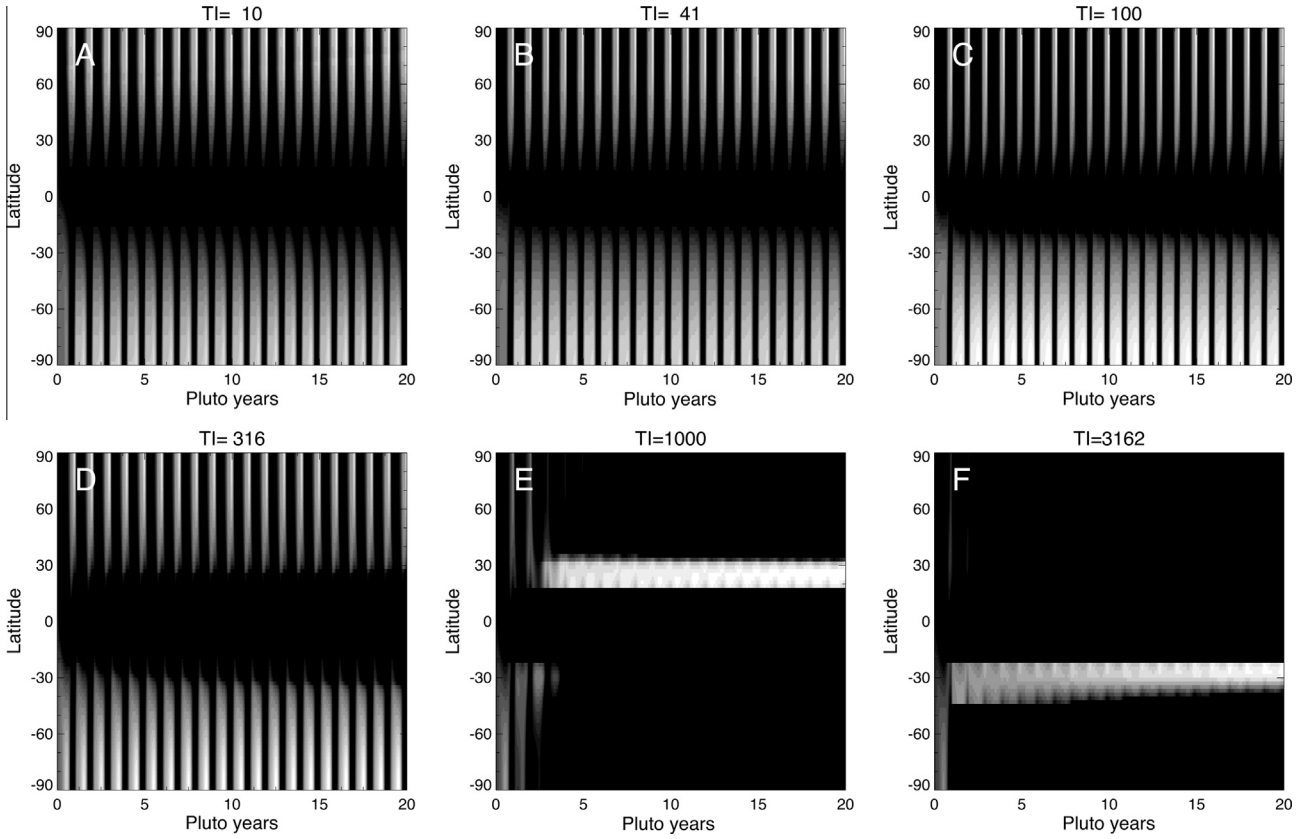

Fig. 5. Predictions of surface ice coverage (black, no ice; white, maximum ice coverage) showing the dependence on the surface thermal inertia. The full 20-year simulations are shown. Thermal inertias are (A) 10, (B) 41, (C) 100, (D) 316, (E) 1000, (F) 3162 in SI units. Conditions for all other parameters (albedo, emissivity, volatile inventory) are equivalent to those from Run #22 from Hansen et al. (2015). Note the transition from polar caps to more tropical ice bands as the thermal inertia is increased (see text for details).

out" on the surface for the majority of the year, with a significant atmosphere only near perihelion (shortly after the beginning of each Pluto year). As thermal inertia is increased, surface pressure at the coldest part of the year slowly increases, until there is only minimal seasonal variation at the largest of thermal inertias sampled (the long dashed line). The surface pressure near perihelion is rather insensitive to the thermal inertia, but for seasons away from that period, there is a very strong dependence on thermal inertia.

Figs. 5 and 6 show the latitudinal extent of surface ice coverage as a function of season for all 20 years of the surface volatile exchange model simulations, illustrating the change in behavior of surface ice accumulation with changes in the thermal inertia. At low thermal inertias, there are essentially alternating polar caps, although the equatorward edge of these caps may well extend into latitudes less than 30°. Northern summer (southern winter) occurs near perihelion and thus the northern polar cap recedes very quickly, leading to the rapid increase and peak in surface pressure

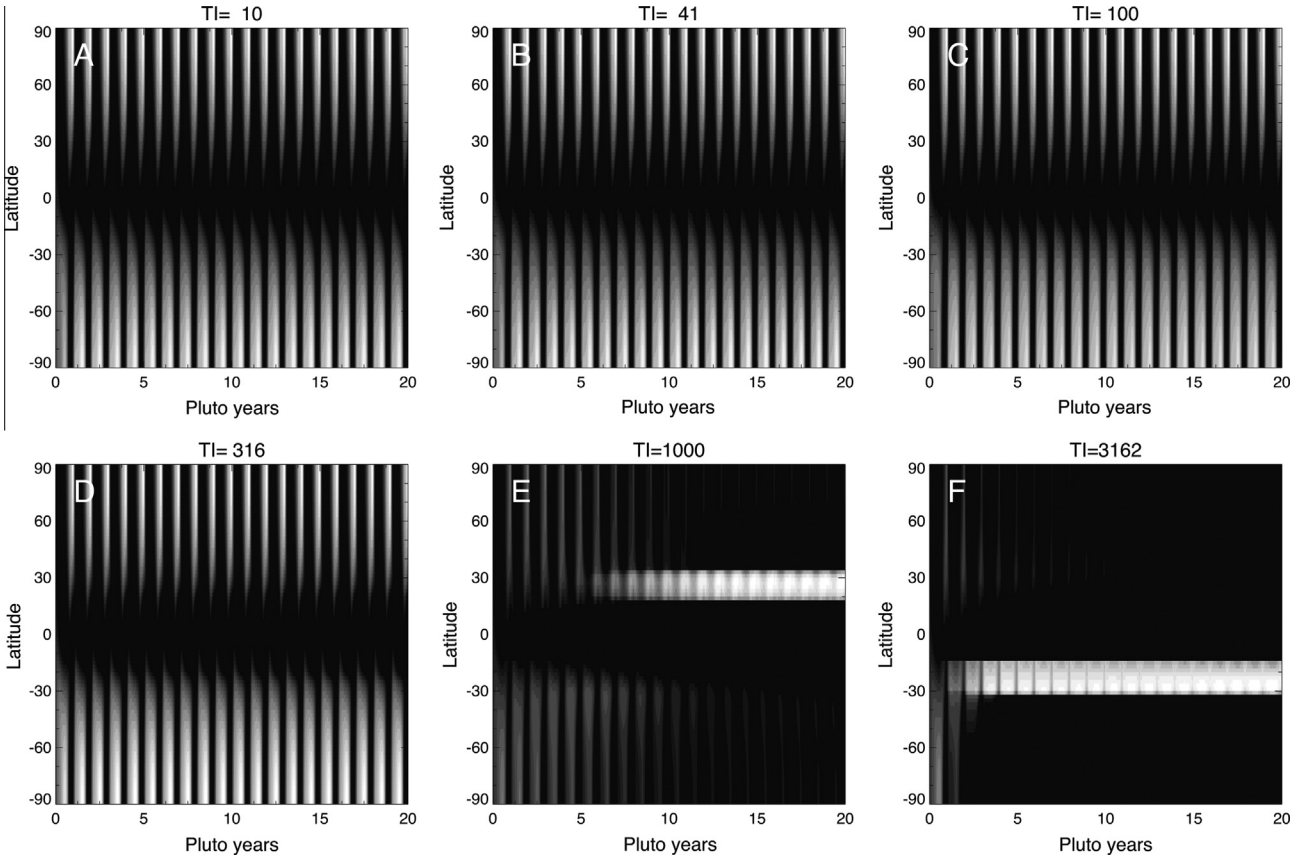

Fig. 6. Same as Fig. 5, except using input parameter conditions equivalent to run PNV9 from Young (2013). Note the transition from polar caps to more tropical ice bands as the thermal inertia is increased (see text for details).

at this period. Southern summer occurs near aphelion, and with Pluto's highly eccentric orbit, southern summer is colder than northern summer. Thus, the recession of the south polar cap is relatively moderate, compared to the north.

Of note as well is the qualitative change in ice coverage behavior as thermal inertia increases to the highest values sampled here. At some value of thermal inertia (likely dependent on the exact values of albedo, emissivity, and total volatile inventory), the alternation of polar ice caps transitions to a long term accumulation of ice near the equator. Pluto has a highly tilted rotation axis, well past the value (around 45–50°) where, on an annual average, the minimum annual insolation occurs at low latitudes rather than the polar regions. With Pluto's minimally absorbing atmosphere, this also implies that the coldest temperatures will also occur at low latitudes, and a permanent "cold finger" of accumulating ice builds in this region.

This remains true in the low thermal inertia simulations. Here, the rapid reaction of surface temperature to changes in insolation favors accumulation of ice at the poles. The latitude of the center of the cold finger also appears to be somewhat dependent on the chosen value of the thermal inertia (panels E and F in Figs. 5 and 6).

We have confirmed that the transition from polar to low-latitude ice accumulations does not result from numerical (computational) instability; Figs. 5E, F, 6E and F show the presence of alternating polar ice caps during the first few years of the simulation, only to trend towards a permanent accumulation of equatorial ice after Pluto several years. Longer simulations (of order 100 Pluto years, not shown) confirm the stability of low-latitude ice accumulations over very long time scales. Similar behavior is described in Hansen and Paige (1996) and Hansen et al. (2015), who also found that large surface thermal inertia values led to the formation of permanent low-latitude zonal bands rather than polar caps. They also mention that the location of the zonal band was not significant, but depends sensitively on initial and boundary conditions, as is the case with our simulations as well.

4. 1D radiative–conductive–convective atmospheric model

A complementary reduced version of the PlutoWRF GCM is the one-dimensional model, where only a vertical profile of the atmosphere is represented, and surface pressure and temperature as a function of time are derived from the surface volatile exchange model of Section 3. Only the radiation parameterization (Zhu et al., 2014, and see Section 2.1) and the vertical turbulence (boundary layer) parameterization (Hong et al., 2006) from the full three-dimensional GCM are used in this version of the model. While a full three-dimensional grid can be specified here as well, only one dimension (the vertical) is used in order to allow for quick and efficient multi-annual simulations. Longitudinal dependence is unnecessary with the use of diurnally averaged insolation and our focus on processes occurring on the seasonal (and not diurnal) timescale. Unlike the case of the two-dimensional surface volatile exchange model, we can also ignore latitudinal dependence, since pole-to-equator temperature differences throughout most of the atmosphere are very small (see Section 5 below) even when larger differences exist in surface temperature. The one-dimensional model then essentially represents a globally-averaged temperature profile, which in any case was the original source of the radiative parameterization in the first place (Zhu et al., 2014). This is a justifiable approximation because the dynamical time scales (e.g.,

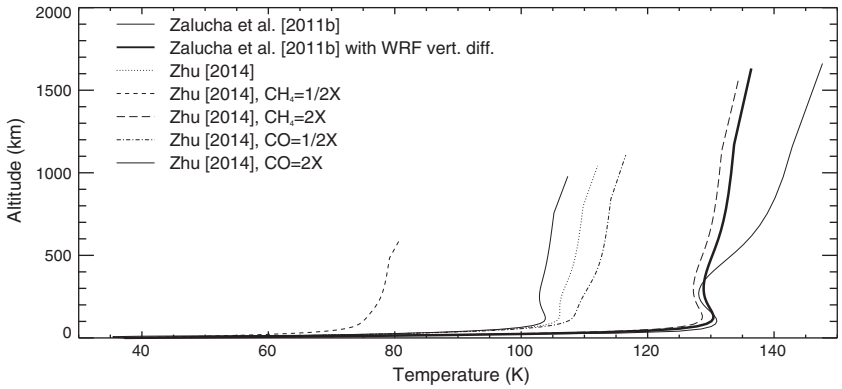

Fig. 7. Predictions of vertical profiles of global average temperature at about the time of *New Horizons* closest approach to Pluto from the one-dimensional model for a series of constant surface pressure and temperature simulations based on the reported values of Zalucha et al. (2011b) and Zhu et al. (2014). The different cases are described in the text.

the time for a parcel of air to go around half the planet, a few sols for a typical wind speed of order a few m/s, see Section 5) is much shorter than the radiative time scale (several hundreds to thousands of sols) (Strobel et al., 1996). The model is also similar to that described in Zalucha et al. (2011a,b), although their purpose was to use their model to match observed occultation light curve profiles.

The advantage of the one-dimensional model is the allowance of an initial exploration of the effects of varying input parameters in an efficient manner, allowing the most significant or interesting choices to be further explored with the full three-dimensional model. An example of this capability is illustrated in Fig. 7, which shows the temperature profiles of several different one-dimensional runs at the end of the simulations, at approximately the time of *New Horizons* closest approach to Pluto. The solid lines shown are simulations that use the lower boundary conditions of temperature and pressure, and minor species mixing ratios, from the "control values" of Zalucha et al. (2011b), but with variations in how turbulent vertical mixing is handled. The thin solid line uses the scheme described in Zalucha et al. (2011b) for calculating vertical eddy diffusion coefficients. The thick solid line uses PlutoWRF's native vertical turbulent mixing scheme (often referred to in the literature as "planetary boundary layer schemes," although they parameterize mixing throughout the model and not just strictly the boundary layer) to calculate turbulent eddy diffusion coefficients, with a local modification in the free atmosphere regime to more accurately simulate behavior seen in terrestrial low pressure altitudes. In the lower atmosphere, there is only a few Kelvin difference at most between the two alternate representations of the vertical turbulent mixing, but the profiles diverge at height. This is likely due to the differences in eddy mixing diffusivity values calculated at these heights between the two schemes. The dashed and dotted lines represent the effect on the thermal profile of variation in the minor species mixing ratios. In these simulations, the lower boundary conditions are those specified in Table 1 of Zhu et al. (2014), and the values of minor species mixing ratios listed there represent the "base" case (the dotted line). Increasing or decreasing the CH_4 mixing ratio by a factor of two (short and long dashed lines, respectively) increases or decreases the temperatures in the thermal profile as well, while increasing or decreasing the CO mixing ratio (dashed with three dots line, and dashed-dotted line, respectively) has an inverse (because CO primarily acts to cool in the infrared), but weaker, effect compared to CH_4. The values of surface pressure and surface temperature and CO mixing ratio are nearly identical in the control case of Zalucha et al. (2011b) and Table 1 of Zhu et al. (2014), while the value of CH_4 mixing ratio in Zalucha et al. (2011b) is approximately 2.4 times that of Zhu et al. (2014), and thus the dark solid line could also be approximately labeled as "Zhu et al. (2014), $CH_4 = 2.4\times$" as well.

The effects of variations in the lower boundary condition that drive the one-dimensional model are explored in Fig. 8, showing runs PNV9, EPP7, EEC7 of Young (2013), and the "best fit" run (Run #22) of Hansen et al. (2015). In three of the four cases, there is still a substantial atmosphere at the time of *New Horizons* closest approach, with atmospheric temperatures roughly in line with those seen in recent occultation-derived profiles. The outlier case, run EEC7, is in the "exchange with early collapse" regime as categorized in Young (2013) and, as the name implies, has essentially no atmosphere at this time in Pluto's orbit.

Fig. 9 shows the seasonal variation of the global-average thermal profile from the one-dimensional model for the set of cases shown in Fig. 8. For all of the cases shown, temperatures decrease strongly away from the perihelion period even when the surface pressure is roughly constant (the high thermal inertial PNV9 case). Temperatures peak near perihelion, but the length of the period for which temperatures are "warm" compared to the non-perihelion season depends on the surface parameters. Even during the "warm" perihelion period, temperatures low in the atmosphere (for altitudes less than about 50 km or so) maintain a strong lapse

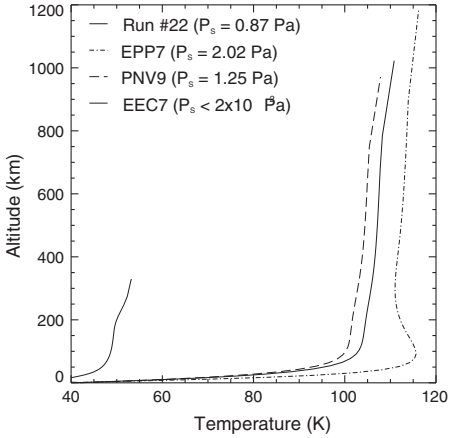

Fig. 8. Predictions of vertical profiles of global average temperature at about the time of *New Horizons* closest approach to Pluto (with the exception of the line labeled EEC7) from the one-dimensional model for the series of "best fit" cases from the two-dimensional surface volatile exchange models of Young (2013) and Hansen et al. (2015). Cases are also labeled with the predicted global average surface pressure derived from the two-dimensional model. The EEC7 simulation has near total atmospheric collapse before the time of *New Horizons* closest approach to Pluto, and so a period in late 2012, before that collapse, is shown.

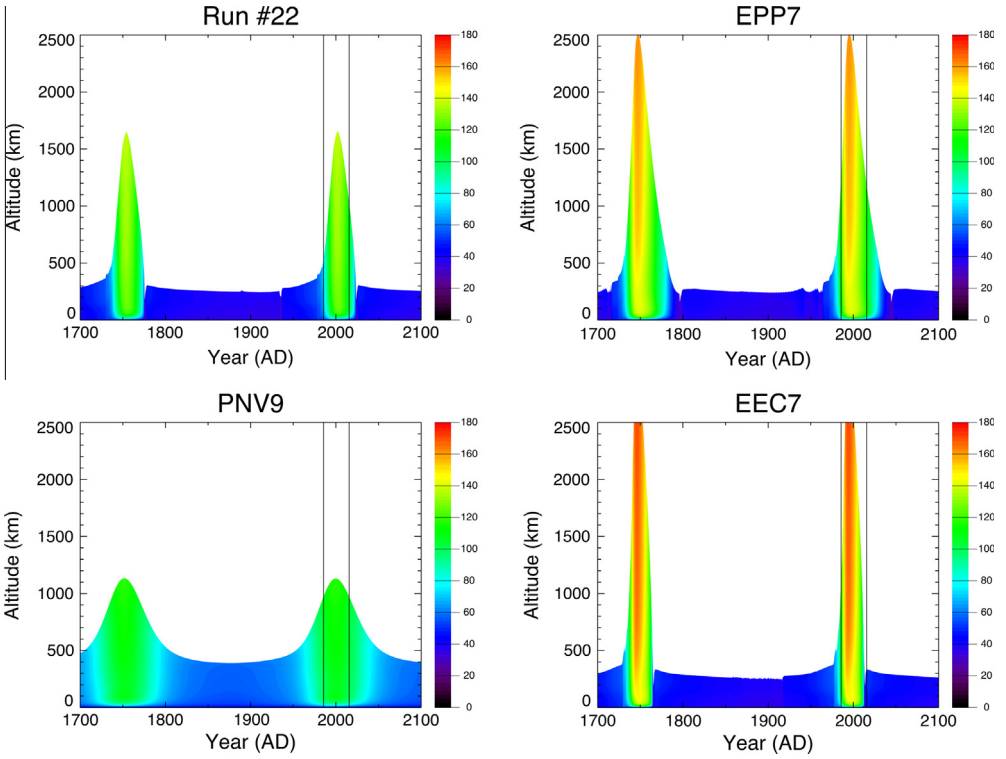

Fig. 9. Global average thermal profile of Pluto's atmosphere as a function of time for different surface input parameters. The solid vertical lines bound the period 1988–2015, approximately the period covering the interval between the discovery of Pluto's atmosphere (and subsequent occultation observations) and the time of *New Horizons* closest approach. The title of each subfigure refers to the source of values of the surface parameters for each specific run: Run #22 of Hansen et al. (2015), and runs PNV9, EPP7, and EEC7 from Table 1 of Young (2013). The mixing ratios of CH_4 and CO used are those of Zhu et al. (2014).

rate, decreasing from an isothermal mid-to-upper atmosphere temperature of 100 K or more, to approximately the seasonal surface ice temperature of about 40 K or less.

5. PlutoWRF general circulation model

Using the capabilities of the previously-described, simplified one- and two-dimensional models, we can now perform full three-dimensional simulations of Pluto's atmosphere without having to include computationally expensive and slow multi-Pluto-year spin-up simulations to allow the atmosphere and surface to come into approximate long-term equilibrium. Although a full exploration of seasonal variations for a realistic suite of physical assumptions must necessarily wait for improved observational constraints (eagerly anticipated from the *New Horizons* flyby), we illustrate the capabilities of our unified modeling approach by investigating the three-dimensional time-dependent atmospheric dynamics and structure for four representative surface volatile exchange models: Run #22 of Hansen et al. (2015), and runs PNV9, EPP7, and EEC7 from Table 1 of Young (2013).

All simulations for these four representative cases encompass a period of about 1800 Pluto sols (approximately 30 Earth years) starting around 1985 (and including a short spin-up period to remove any perturbations from incompletely balanced initial conditions) through northern spring equinox, perihelion, and ending near the time of *New Horizons* closest approach in 2015. Full diurnal variability is now included in these three-dimensional model simulations, as diurnal averaging was only used in the multi-annual two- and one-dimensional boundary and initial condition-determining simulations for computational efficiency.

5.1. Run #22

Run #22 was the "best fit" simulation from Hansen et al. (2015) to a variety of observational constraints. We also find similar behavior in our two-dimensional surface volatile exchange model, and temperatures as predicted in the one-dimensional model are also roughly in line with radial temperature profiles retrieved from occultations observations.

Fig. 10 shows results from the full period of the three-dimensional PlutoWRF GCM simulation using the surface and initial conditions with parameters consistent with those of Run #22. Surface pressures undergo more than an order of magnitude change over this period, and are very consistent with the results of the two-dimensional surface volatile exchange model. Surface ice starts out with a broad northern hemisphere seasonal cap with slowly erodes to begin forming a seasonal cap at the south pole throughout the simulation period. The global-average temperature profile is approximately 20 K warmer than what is seen in occultation retrievals, and the predicted times of peak temperature (and largest atmospheric extent) vary slightly between the three-dimensional and one-dimensional models, likely due to the effect of dynamics and coupled surface model in the three-dimensional model.

Results from the end of the simulation, around the time of *New Horizons* closest approach to Pluto, are shown in Fig. 11. Vertical temperature profiles are broadly isothermal throughout most of the atmosphere, with a sharp decrease in temperature towards the cold surface at all latitudes, consistent with profiles derived from occultation observations (Elliot and Young, 1992; Elliot et al., 2003, 2007; Young et al., 2008; Zalucha et al., 2011a,b). Winds are dominated by the volatile flow as the warming north polar cap sublimes and air is deposited on the growing south polar

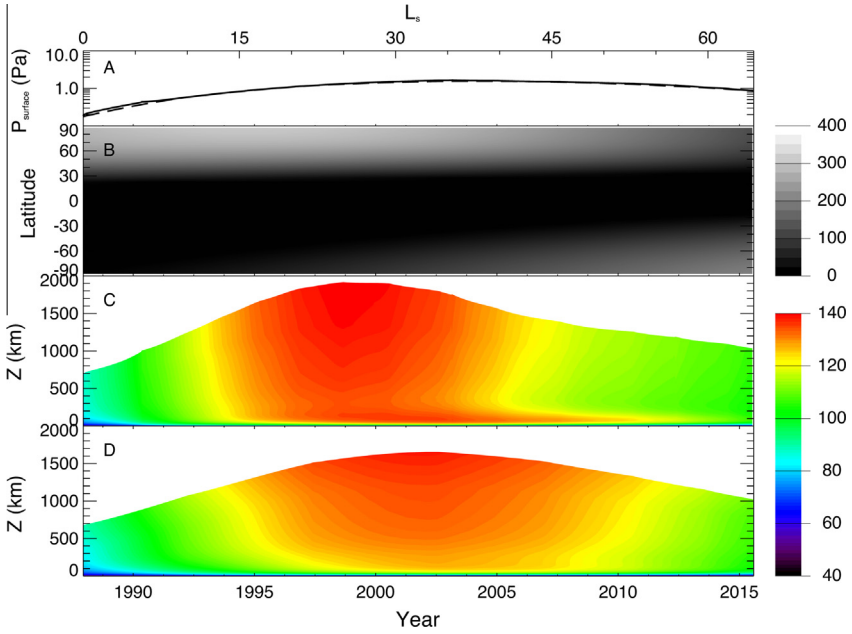

Fig. 10. Plots of (A) global-average surface pressure, (B) zonal-average surface ice distribution (scale bar to right indicates surface ice density in kg/m^2), (C) global-average vertical temperature profile (scale bar to right indicates air temperature in K) from a three-dimensional PlutoWRF GCM simulation with surface condition parameters are equivalent to those of run Run #22 of Hansen et al. (2015). A comparison with the results from the one-dimensional model (seen in Fig. 9) covering the same period as the three-dimensional simulation are plotted (scale bar to right indicates air temperature in K) in subfigure (D) for ease of comparison with the approximately equivalent three-dimensional quantity in subfigure (C). Additionally, in subfigure (A), the global-average surface pressure from the three-dimensional GCM simulation (solid line) is in excellent agreement with the two-dimensional surface volatile exchange model (barely distinguishable dotted line).

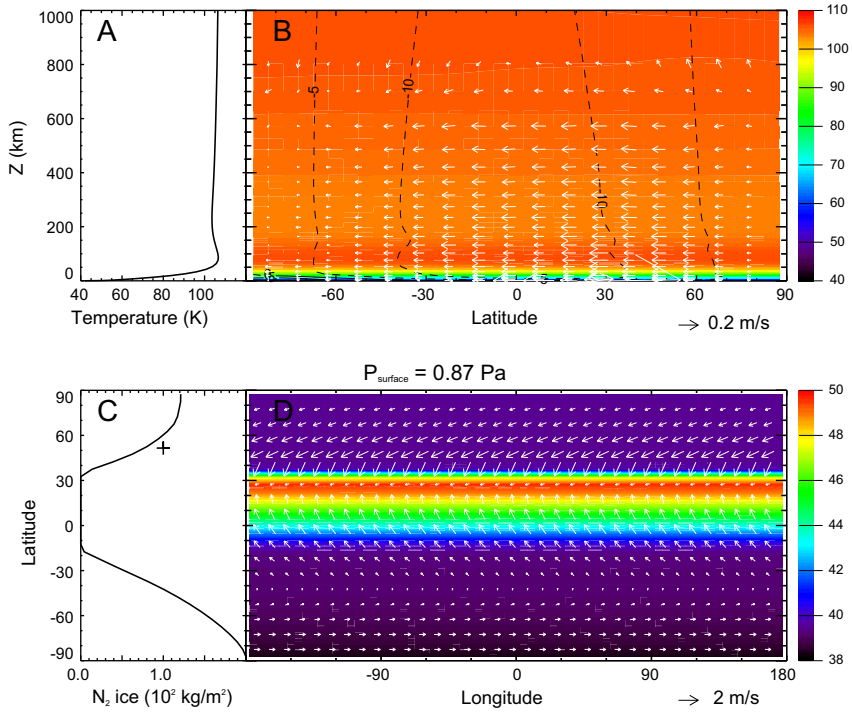

Fig. 11. Simulation of conditions at the time of *New Horizons* closest approach to Pluto, from a PlutoWRF simulation using the initial conditions as specified from the two-dimensional surface volatile exchange model, a thermal profile derived from the one-dimensional model using mixing ratios specified in Zhu et al. (2014), and winds initially at rest. Surface condition parameters are equivalent to those of run Run #22 of Hansen et al. (2015). (A) Diurnal- and global-average (area-weighted) temperature profile. (B) Diurnal- and zonal-average temperature and wind profiles. Temperature is shown as the background colors, black contours are magnitude of the zonal (east–west) wind (positive values are solid lines, negative values are dashed lines), and the arrows are the meridional (north–south) and vertical winds (scaled by a factor of 10) expressed together as a vector. (C) Diurnal- and zonal-average ice coverage. The "+" symbol shows the subsolar latitude at the current season. (D) Map of near-surface diurnal-average air temperature and near-surface winds. Temperature is shown as background colors, and arrows are near-surface horizontal winds (with the largest arrow scaled to the magnitude indicated in the legend below the subfigure).

cap, which is larger than the north cap at this time, and extends nearly to the equator. Zonal winds are also dominated by the effect of this flow as they conserve angular momentum in their trip from north to south, and thus have a negative (westward) magnitude over the equator. Winds near the surface are more influenced by surface conditions, and show a flow towards a low pressure region created by the higher temperature, ice-free surface at low latitudes.

Surface wind streaks, if present, could potentially be visible to cameras on *New Horizons*. They may have been emplaced in previous seasons, and Figs. 12–14 (and including Fig. 11 as the last member of the sequence) show the changes in Pluto's atmosphere (as predicted in this simulation) at roughly equal intervals from the beginning of the simulation to the end. For most of this period the larger temperature difference from the ice-free surface to the cold north polar cap sets up a jet whose influence can also be seen weakly in the near-surface winds. As the south polar cap grows, near-surface winds slowly change to the pattern seen in Fig. 11, with a convergence to the warm equatorial ice-free region. As the atmosphere deflates, the jet also breaks up and settles into the angular-momentum-conserving pattern seen in Fig. 11.

The pattern of the simulated zonal-average zonal winds at these periods is illustrated again in Fig. 15, which also shows the magnitude of the zonal (east–west) component of the gradient wind. The gradient wind was estimated from the zonal-average temperature profiles assuming gradient wind balance in the horizontal and hydrostatic balance in the vertical, using the relation (e.g., Andrews et al., 1987):

$$\frac{\partial}{\partial p}\left(\bar{u}f + \bar{u}^2\frac{\tan\phi}{a}\right) = \frac{R}{pa}\frac{\partial \overline{T}}{\partial \phi},$$

where p is pressure, f is the Coriolis parameter, ϕ is latitude, a is the planetary radius, R is the atmospheric gas constant, T is temperature, u is zonal wind, and an overbar means a zonal-averaged quantity. The equation is integrated upwards in altitude with an assumption of zero winds at the surface; results poleward of 15° are not integrated due to the singularity in solutions to the equation at $\phi = 0$, and the results are shown as the dashed lines in Fig. 15. For most of the period of simulation, forcing of the zonal winds is dominated by a thermal wind balance derived from the pole-to-equator temperature differences, shown in Fig. 16, which in general are very small ($\leqslant$1 K). Gradient wind balance was also observed very near the poles in Zalucha and Gulbis (2012). At the same time however, there is also a forcing from the sublimation flow as the sunlit seasonal polar cap slowly sublimes and the seasonal cap at the opposite, constant-night, pole grows. As the pole-to-equator temperature difference declines due to the progressing of seasons, the continuing sublimation flow remains, becoming the dominant contribution to the zonal winds, which develop in response to an angular momentum balance as air moves from one hemisphere to the other.

5.2. EPP7

Run EPP7, shown in Fig. 1 of Young (2013), is in the "exchange with pressure plateau" category. This category has polar caps at both poles for an extended period after perihelion, as we also find with this simulation. (Run #22 of Hansen et al. (2015) would broadly fit in this category as well.)

EPP7 is roughly similar to Run #22 in terms of surface ice distribution (Fig. 17), starting off with a large northern polar cap that slowly sublimes while the southern polar cap grows during this period. Surface pressures are slightly larger than in Run #22 due to the larger inventory of N_2. The global-average temperature profile is a few tens of K warmer than what is typically seen in occultation retrievals, particularly closer to perihelion. The predicted time of peak temperature (and largest atmospheric extent) varies only slightly between the three-dimensional and one-dimensional models compared to Run #22.

Conditions at the time of *New Horizons* closest approach are also broadly similar to those of Run #22, with general north-to-south sublimation air flow, and the subsequent forcing of zonal winds

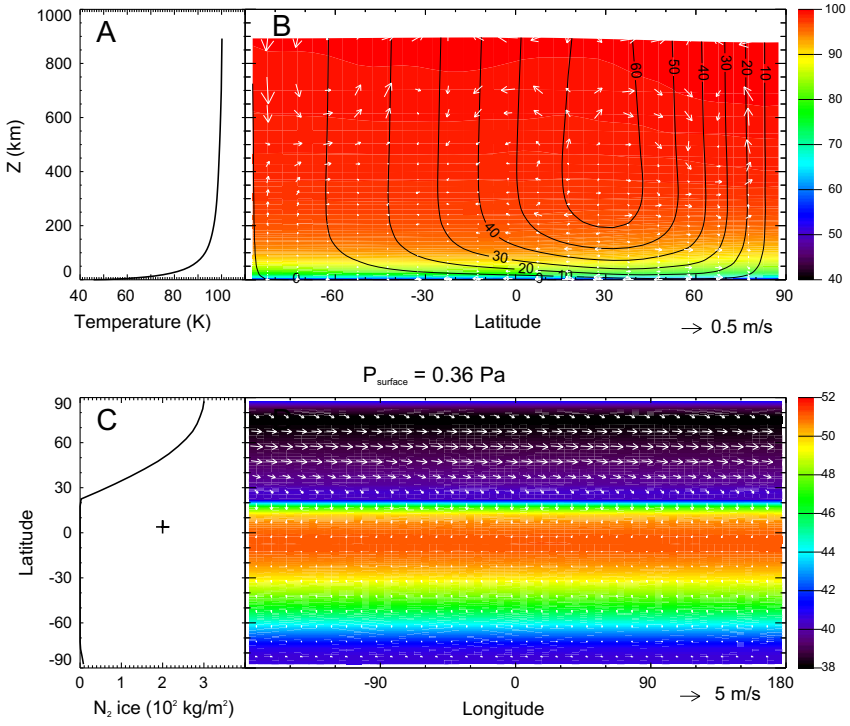

Fig. 12. Same as Fig. 11, except for a period around September 1989.

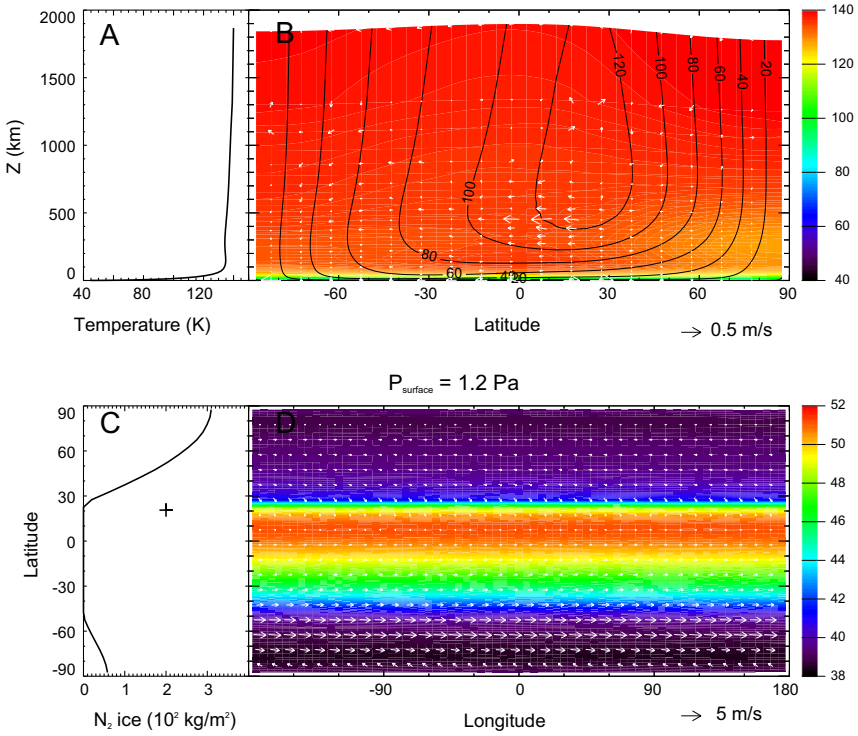

Fig. 13. Same as Fig. 11, except for a period around July 1997.

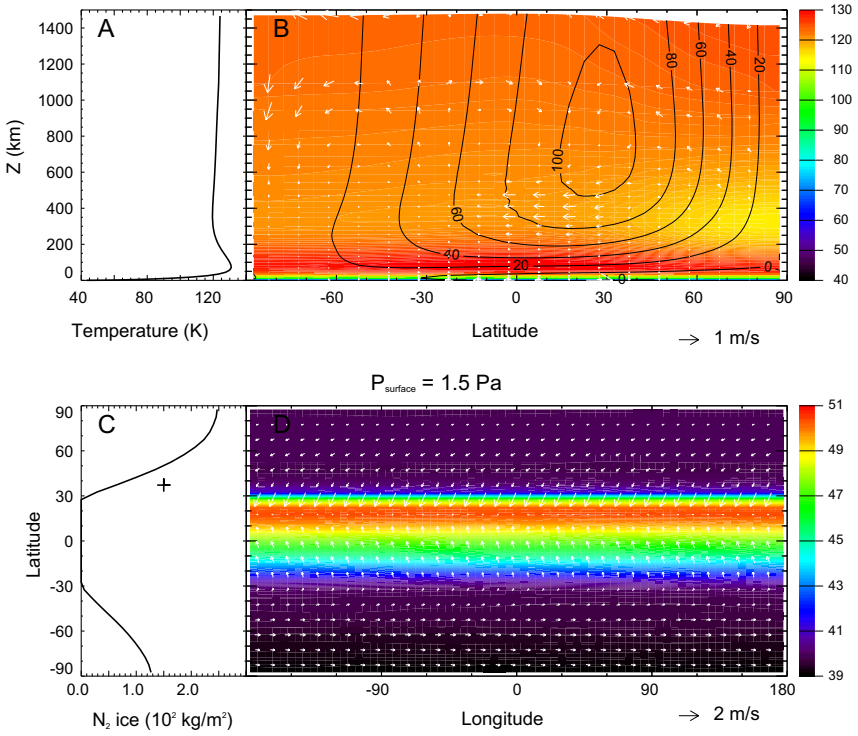

Fig. 14. Same as Fig. 11, except for a period around February 2006.

as a result of the conservation of angular momentum as air crosses the equator (Fig. 18). The dominant thermal wind balance of zonal winds at earlier periods is also broadly consistent with Run #22 (not shown). Near-surface wind patterns at this period are also similar, but with speeds slightly weaker compared to Run #22.

5.3. PNV9

Run PNV9 comes from the "permanent northern volatiles" category in Young (2013) (and shown in Fig. 1 there) although, as discussed previously, after a Plutonian decade or so, our surface

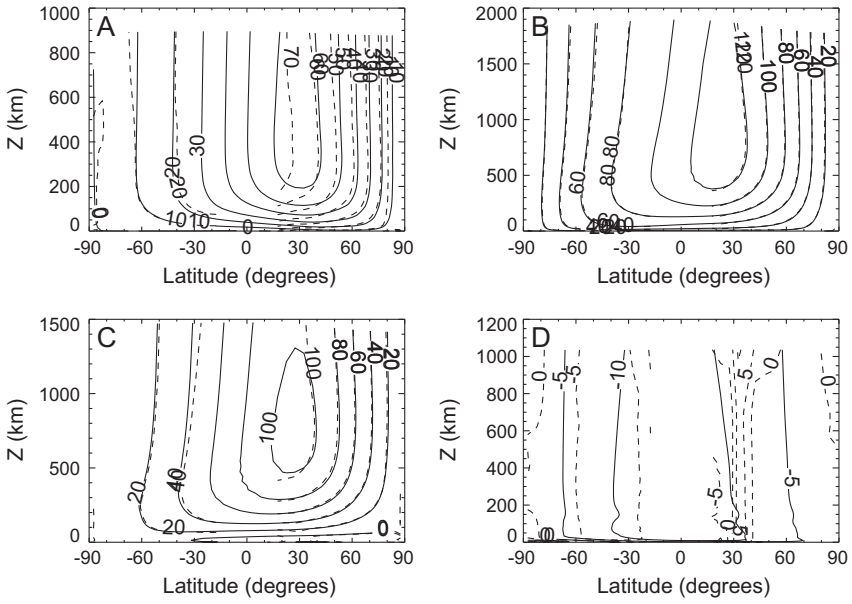

Fig. 15. Zonal-average zonal (east–west) winds as predicted by the PlutoWRF simulation shown in Figs. 11–14 (solid lines) and the derived gradient wind from the zonal-average temperature profiles from the same periods (dashed lines). Gradient winds are not calculated equatorward of 15°. Approximate periods shown are (A) September 1989, (B) July 1997, (C) February 2006, and (D) July 2015.

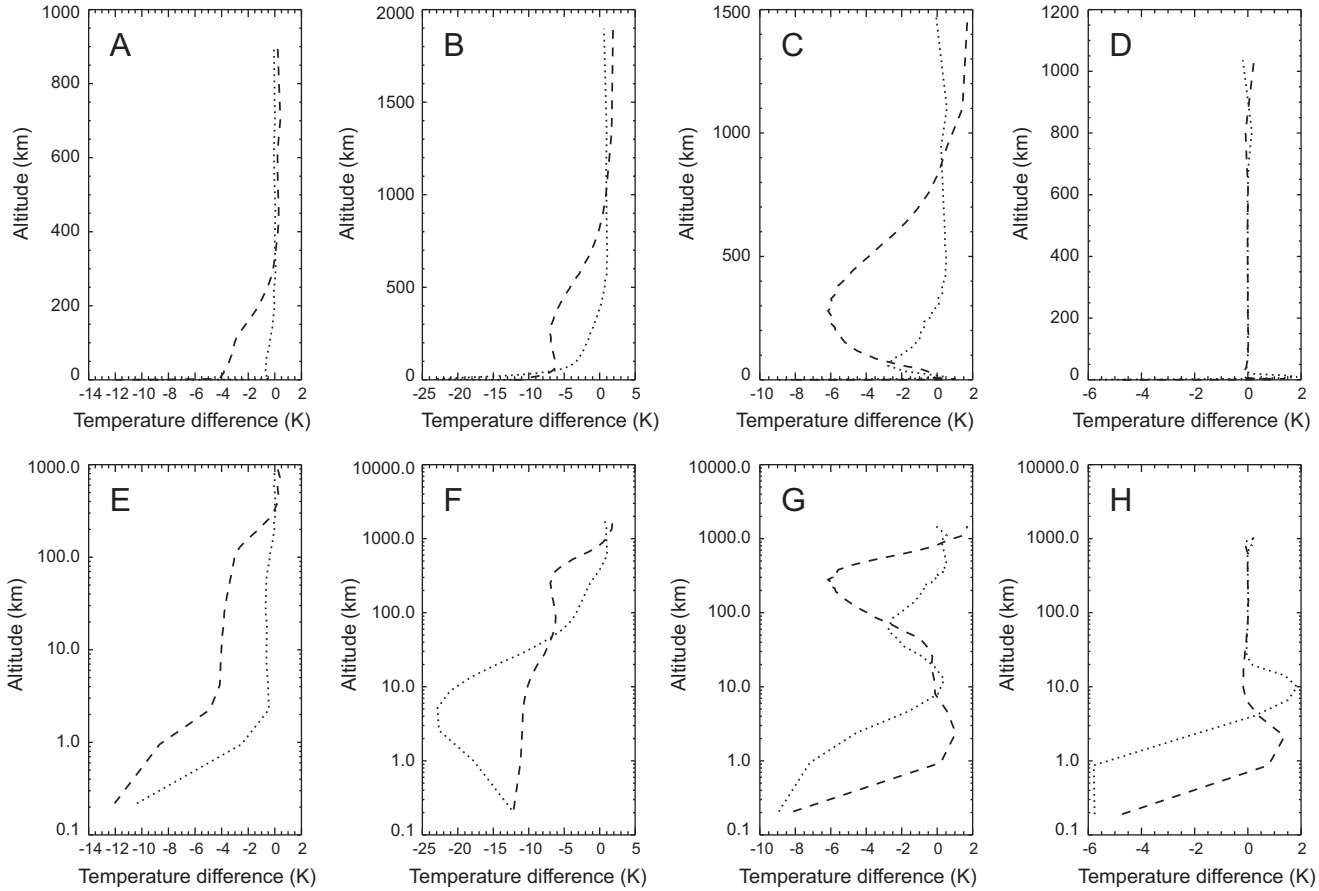

Fig. 16. Pole-to-equator temperature differences on Pluto, as predicted by the PlutoWRF simulation shown in Figs. 11–14. Temperature differences from the equatorial thermal profile for the zonal-average thermal profile of the grid points nearest the south pole (dotted line) and north pole (dashed line) are plotted. Subfigures (A)–(D) are for the same periods as in Fig. 15A–D, respectively, and subfigures (E)–(H) are the same data as subfigures (A)–(D) (respectively), but plotted with a logarithmic vertical axis to highlight the differences near the surface.

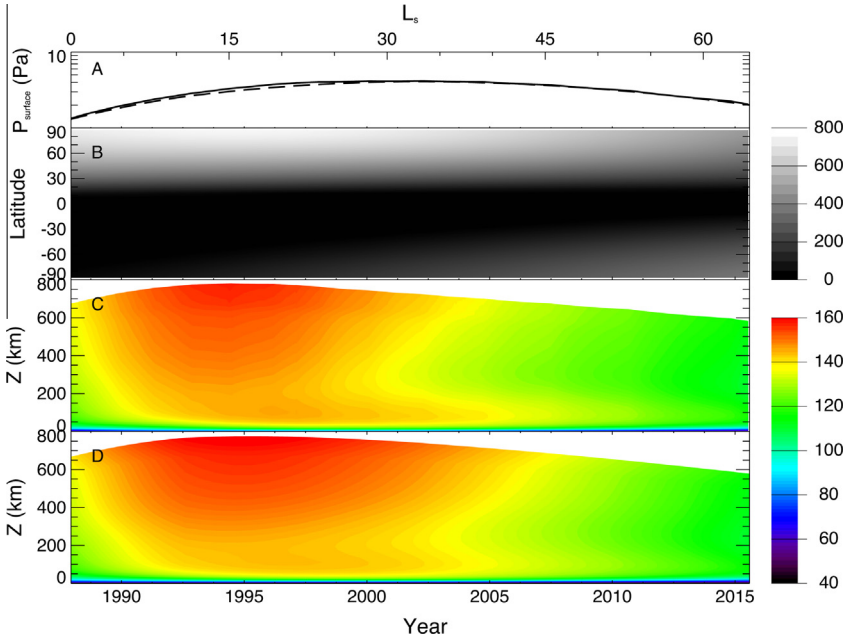

Fig. 17. Same as Fig. 10, except surface condition parameters are equivalent to those of run EPP7 of Young (2013).

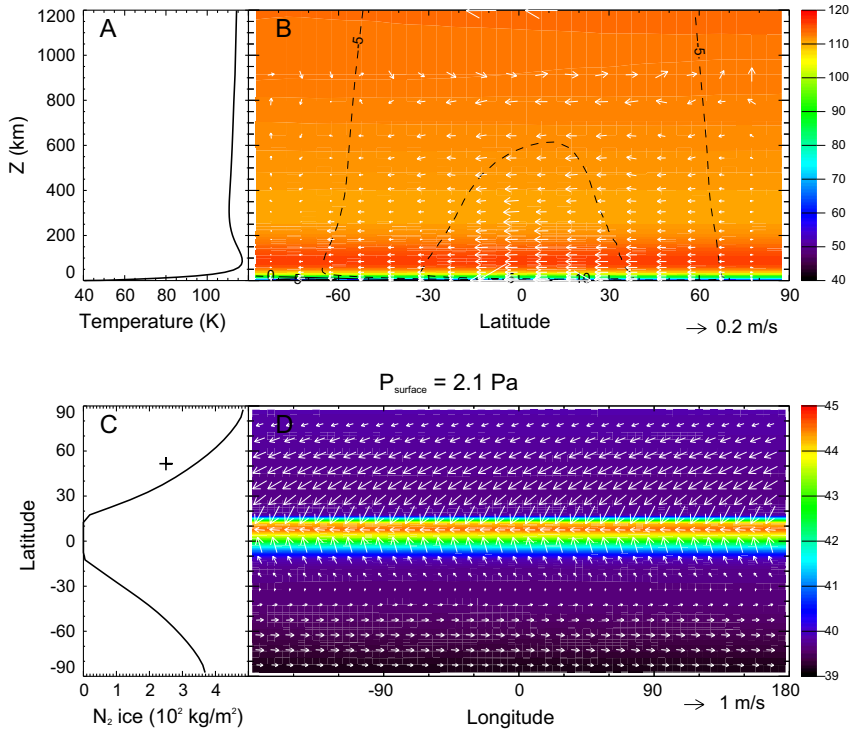

Fig. 18. Same as Fig. 11, except surface condition parameters are equivalent to those of run EPP7 of Young (2013).

volatile exchange model predicts all ice moving to a permanent low-latitude band, the exact extents of which are dependent on the thermal inertia and volatile inventory chosen. (In this sense the label of "permanent northern volatiles" to this case is misleading and inappropriate.) The permanent (and thick) low-latitude band of ice keeps pressures nearly constant throughout the year, as relatively smaller amounts of sublimation occur at the edges of this band as the sun moves from solstice to solstice.

During the period of the GCM simulation, surface pressure changed only by a factor of two or so (Fig. 19) compared to the order-of-magnitude changes that occur in the other cases. The pressure changes result from subtle changes in the location of the edges of the low-latitude zonal ice band. These are small compared to the total ice cap size, and so the effect is barely visible in the zonal-average ice plot (Fig. 19B). The global-average temperature profiles are very similar to those typically seen in occultation retrievals throughout this period. The predicted time of peak temperature (and largest atmospheric extent) shows a small offset (a few Earth years), as was also seen in the EPP7 simulation.

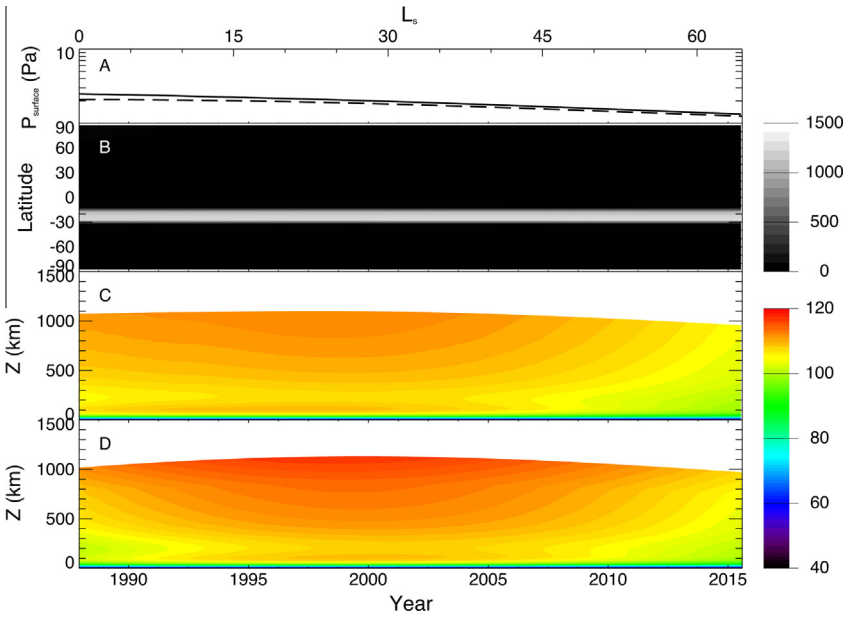

Fig. 19. Same as Fig. 10, except surface conditions parameters are equivalent to those of run PNV9 of Young (2013). See text for a discussion of the low-latitude bands of the ice deposits in our models, in contrast to the north polar regions found by Young (2013).

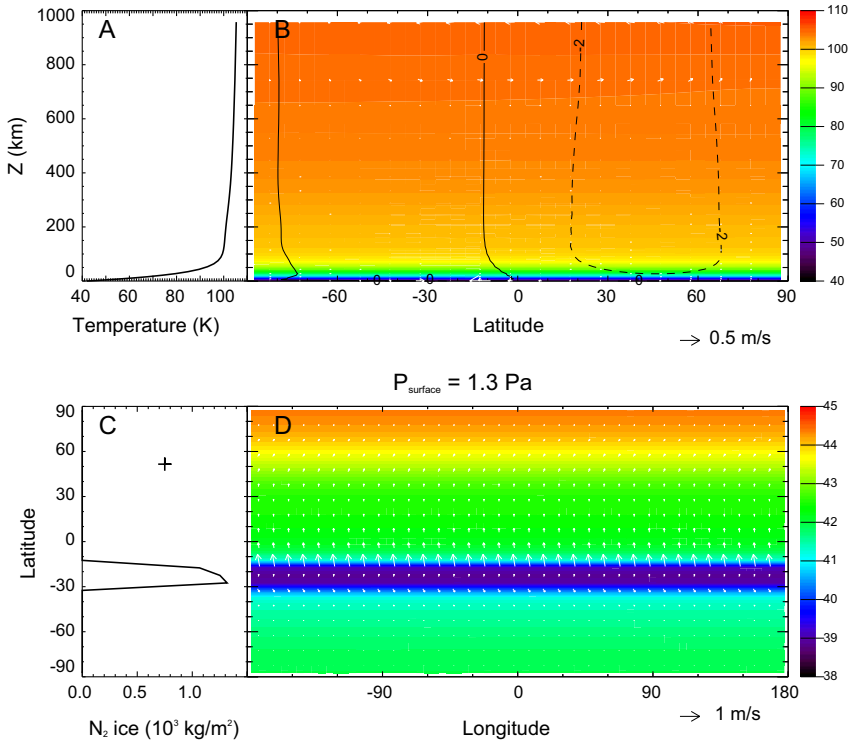

Fig. 20. Same as Fig. 11, except surface condition parameters are equivalent to those of run PNV9 of Young (2013).

Predicted near-surface winds at the time of *New Horizons* closest approach (Fig. 20D) are almost the inverse of Run #22 or EPP7, with winds blowing away from the equatorial icy region, which, while cold on an annual basis, is in sunlight during the day (see subsolar latitude mark in Fig. 20C) and is thus subliming at this season. Zonal winds are very weak, and still show some small forcing from a thermal wind balance pattern, although the pole-to-equator temperature differences are very weak compared to the previous two simulations, due to the lack of seasonal polar caps in our PNV9 simulations and the presence of a long-lived low-latitude band of ice-covered surface.

5.4. EEC7

Run EEC7 is in the "exchange with early collapse" category of Young (2013) (and shown in Fig. 1 there), and included those simulations that lost their northern volatile caps shortly after perihelion. This category contained simulations with nearly total

atmospheric collapse by the time of *New Horizons* closest approach, a result that we see as well. Indeed, in our GCM simulation of this case, the simulation ends earlier (around 2012) than the full period of the other simulations (all the way to 2015) due to the orders-of-magnitude drop in surface pressure and subsequent loss of model accuracy under those extreme conditions. We similarly find that the northern volatile cap disappears more quickly than the other cases, but is still present throughout most of the period of our simulation.

Surface pressure changes over the first half of the simulation period are of similar magnitude to the other runs (Fig. 21A), but are followed by a very quick drop over a very short period (a few Earth years or a couple hundred Pluto sols). The global-average temperature profiles also get quite warmer (many tens of K), likely

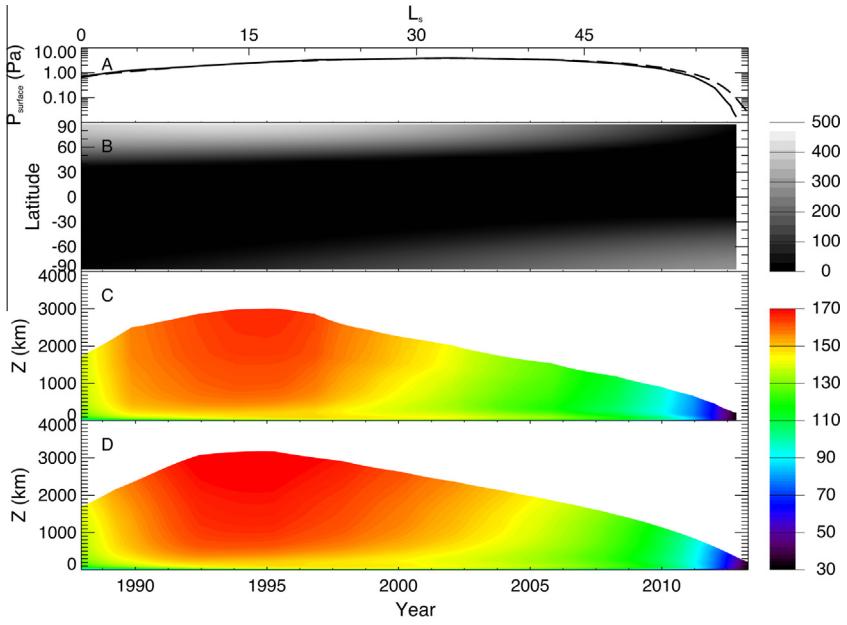

Fig. 21. Same as Fig. 10, except surface condition parameters are equivalent to those of run EEC7 of Young (2013), and only showing results until a period in late 2012 when the simulation ends due to near total collapse of the atmosphere.

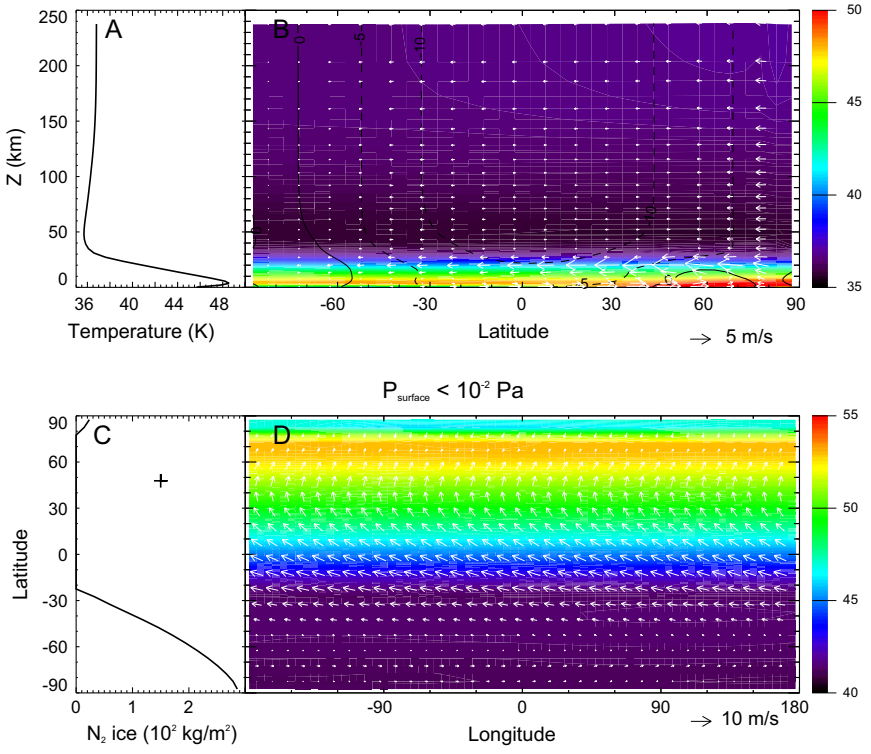

Fig. 22. Same as Fig. 11, except surface condition parameters are equivalent to those of run EEC7 of Young (2013) and for a period in late 2012 right before the simulation ends when the atmosphere collapses.

due to the greater vertical extent and subsequent heating of the atmosphere, in this case compared to occultation retrievals for quite an extended period around perihelion, and then quickly cool as both the air mass drops and Pluto recedes from the sun.

Fig. 22 shows the atmospheric conditions right before the simulation ended due to extreme low surface pressure (many orders of magnitude less than the peak pressure). The temperature profile is cold (but still isothermal) throughout the upper atmosphere, with an increase to the now relatively warmer surface. Air flow is still generally a sublimation flow away from the remnant of the northern polar cap to the growing southern cap, and as we found also for the Run #22 and EPP7 simulations at nearly similar periods, zonal winds show the dominant forcing from conservation of angular momentum as air crosses the equator. The dominant thermal wind balance of zonal winds at earlier periods (not shown) is also similar to that seen in the Run #22 and EPP7 simulations. Near-surface winds show those zonal wind patterns extending to the surface near the equator, and with a Coriolis turning of that wind in the northern hemisphere, and very gentle winds in the southern hemisphere.

6. Discussion and conclusions

Pluto's atmospheric dynamics occupy an interesting regime in which the radiative time constant is quite long, the combined effects of high obliquity and a highly eccentric orbit can produce strong seasonal variations in atmospheric pressure, and the strong coupling between the atmosphere and volatile transport on the surface results in atmospheric flows that are quite sensitive to surface and subsurface properties that at present are poorly constrained by direct observations. In anticipation of the *New Horizons* encounter with the Pluto system in July 2015, we have developed a Pluto-specific three-dimensional GCM, PlutoWRF, built on the foundation of the strong heritage of the WRF and planetWRF models, incorporating the most accurate current radiative transfer models of Pluto's atmosphere, a physically sound treatment of N_2 volatile transport, and the flexibility to accommodate richly detailed information about the surface and subsurface conditions as new data become available.

Given the long seasonal timescales for volatile migration, and the strong feedback between surface albedo, frost deposition, and atmospheric flow, traditional spin-up methods to initiate GCM calculations are computationally demanding for Pluto. We employ an alternative initialization scheme that solves for a physically self-consistent, equilibrated combination of surface, subsurface, and atmospheric conditions to specify the boundary conditions and initial state values for each three-dimensional GCM run. This is accomplished using two reduced versions of PlutoWRF: a two-dimensional surface volatile exchange model to specify the properties of surface N_2 ice and the initial atmospheric surface pressure, and a one-dimensional radiative–conductive–convective model that uses the two-dimensional results to determine the corresponding mean global atmospheric thermal profile. This unified modeling approach is computationally efficient, and tests using the full three-dimensional GCM confirm that further spin-up time using this scheme to correct for initial imbalances requires only a small fraction of a Pluto year.

The underlying physical model of our two-dimensional surface volatile exchange code closely resembles that of Hansen and Paige (1996), Young (2013) and Hansen et al. (2015). Our implementation predicts both the location of surface ice and atmospheric surface pressure values and trends that generally agree quite well with these published results. A notable exception concerns case PNV9 of Young (2013), for which we find a quite different surface ice distribution. Rather than finding a permanent north polar cap (justifying the category name of "permanent northern volatiles" in that work), our results show the development of a low-latitude permanent ice band. This appears to be the equilibrium final state of a system that starts with cycling seasonal polar ice caps, and is a primarily a function of surface thermal inertia as our sensitivity experiments explored. We suspect that the time span of the integration in Young (2013) was too short (only a few Pluto years) for this transition from an initial north polar cap to an equatorial band to emerge. Hansen and Paige (1996) and Hansen et al. (2015) comment that they also find low-latitude ice for high thermal inertial values in their models.

Our one-dimensional model resembles in some respects other published models for Pluto (Strobel et al., 1996; Zalucha et al., 2011a,b; Zhu et al., 2014), but our focus is on providing a self-consistent global atmospheric mean state to our three-dimensional GCM, given the time-dependent lower boundary conditions derived from the two-dimensional surface model just discussed. Our version is a combination of native WRF parameterizations of the boundary layer and free atmosphere (the convective component) with the most up-to-date version of the radiation parameterization of Zhu et al. (2014) (the radiative component). Tests of the reliability of the model show that the inclusion of the Zhu et al. (2014) radiative parameterization reasonably reproduces the rates reported there.

We illustrate the capabilities of PlutoWRF in predicting Pluto's general circulation, thermal state, and volatile transport of N_2 by calculating the three-dimensional dynamical response of Pluto's atmosphere, based on four quite different idealized models of Pluto's surface ice distribution: cases EPP7, PNV9, and EEC7 of Young (2013), and Run #22 of Hansen et al. (2015), their favored model based on comparisons with stellar occultation and other data. In previous work, we explored the seasonal dynamics of atmospheric thermal tides for these same idealized surface models (French et al., 2015), which assume longitudinally-uniform ice distributions.

Our GCM runs typically span a period of 30 Earth years, from 1985 to 2015, from the discovery of Pluto's atmosphere to the *New Horizons* era of high-resolution Pluto observations. In general, for most periods simulated, zonal winds are strongly forced by a thermal wind balance, relaxing in latter years to an angular momentum conservation balance of the seasonal polar cap sublimation flow. Near-surface winds generally follow a sublimation flow from the sunlit polar cap to the polar night cap, with a Coriolis turning of the wind as the air travels from pole to pole. A singular exception is our simulation of the PNV9 case, with its low-latitude ice band, where we find weaker winds and a diurnal sublimation wind as the ice band sublimes poleward during the day and redeposits equatorward at night. The sublimation flow prevents the development of a "Hadley-like" circulation, in the sense that there is no return flow at high altitudes of the low altitude transport. Instead, the circulation is not "closed" as the air is essentially created in one hemisphere and removed in another, and vertical winds, though not completely absent, are generally very small. In all GCM runs, the globally-averaged temperature profiles very closely resemble the results of the one-dimensional model, as expected, with the added ability in the three-dimensional model to express latitudinal variations driven by dynamics and varying solar insolation.

Predictions of atmospheric temperatures from our GCM simulations are similar to those of the model of Zalucha and Michaels (2013). Both models predict nearly isothermal vertical temperature profiles in the upper atmosphere, decreasing to near equilibrium temperatures at the surface, and weak latitudinal temperature differences. Our predicted pole-to-equator atmospheric temperature differences, though small compared to the mean temperature, are nevertheless capable of generating zonal winds in

near complete agreement with a gradient wind balance (see Fig. 16). When these atmospheric temperature gradients are reduced away from the perihelion season, zonal winds are measurably present, and result from a conservation of angular momentum as air is transported from one hemisphere to the other. Meridional (and to a much lesser extent vertical) winds are also primarily forced by this cross-equatorial volatile transport in all seasons examined. Indeed, the wind regimes in all of our GCM simulations differ notably from any of those of Zalucha and Michaels (2013), whose model was initialized and executed with different assumptions (e.g., no ice deposition or volatile transport, a simpler methane-only radiative parameterization, globally uniform surface properties, and a shorter "spinup" period to start the model integration). In our PlutoWRF simulations, volatile transport contributes importantly to the atmospheric circulation, and N_2 sublimation and deposition play a significant role in controlling the heat balance and thermophysical properties of the surface. It is not surprising, therefore, that our GCM results show very different dynamical circulation patterns.

We now have the tools in hand to investigate a host of interesting questions about Pluto's atmospheric dynamics, from explorations of diurnal tides and vertically propagating waves to seasonal variations in surface pressure, frost distribution, and surface and upper atmospheric winds. The results presented here are necessarily idealized, because we do not yet have detailed knowledge of regional variations in Pluto's albedo, thermal inertial, frost composition and depth, among other important lacunae. Nevertheless, to the extent that they do resemble Pluto's actual conditions, they are useful diagnostics, and they illustrate the sensitivity of atmospheric dynamics to the surface frost distribution and the thermal inertia. As *New Horizons* data become available, it will be exciting to use PlutoWRF to construct more physically realistic models of Pluto's atmospheric dynamics and surface wind regimes, and to compare these predictions with possible evidence of aeolian features in high resolution images of Pluto's surface.

Acknowledgment

This work was supported in part by NASA's Planetary Atmospheres Program Grant NNX11AD83G.

References

Andrews, D.G., Holton, J.R., Leovy, C.B., 1987. Middle Atmosphere Dynamics. Academic Press Inc., Orlando, FL.
Bosh, A.S. et al., 2015. The state of Pluto's atmosphere in 2012–2013. Icarus 246, 237–246.
Brosch, N., 1995. The 1985 stellar occultation by Pluto. Mon. Not. R. Astron. Soc. 276, 571–578.
Elliot, J.L. et al., 2003. The recent expansion of Pluto's atmosphere. Nature 424, 165–168.
Elliot, J.L. et al., 1989. Pluto's atmosphere. Icarus 77 (1), 148–170.
Elliot, J.L. et al., 2007. Changes in Pluto's atmosphere: 1988–2006. Astron. J. 134, 1–13.
Elliot, J.L., Young, L.A., 1992. Analysis of stellar occultation data for planetary atmospheres. I – Model fitting, with application to Pluto. Astron. J. 102, 991–1014.
French, R.G. et al., 2015. Seasonal variations in Pluto's atmospheric tides. Icarus 246, 247–267.
Hansen, C.J., Paige, D.A., 1996. Seasonal nitrogen cycles on Pluto. Icarus 120 (2), 247–265.
Hansen, C.J., Paige, D.A., Young, L.A., 2015. Pluto's climate modeled with new observational constraints. Icarus 246, 183–191.
Holler, B.J. et al., 2014. Evidence for longitudinal variability of ethane ice on the surface of Pluto. Icarus 243, 104–110.
Hong, S.Y., Noh, Y., Dudhia, J., 2006. A new vertical diffusion package with an explicit treatment of entrainment processes. Mon. Weather Rev. 134 (9), 2318–2341.
Hubbard, W.B. et al., 1988. Occultation evidence for an atmosphere on Pluto. Nature 336, 452–454.
Olkin, C.B. et al., 2015. Evidence that Pluto's atmosphere does not collapse from occultations including the 2013 May 04 event. Icarus 246, 220–225.
Owen, T.C. et al., 1993. Surface ices and the atmospheric composition of Pluto. Science 261, 745–748.
Person, M.J., 2013. Trends in Pluto's atmosphere from stellar occultations. In: The Pluto System on the Eve of Exploration by New Horizons: Perspectives and Predictions. JHU/APL, Laurel, MD (July 22–26).
Richardson, M.I., Toigo, A.D., Newman, C.E., 2007. PlanetWRF: A general purpose, local to global numerical model for planetary atmospheric and climate dynamics. J. Geophys. Res. 112, E09001. http://dx.doi.org/10.1029/2006JE002825.
Skamarock, W.C. et al., 2008. A Description of the Advanced Research WRF Version 3. Tech. Rep. NCAR/TN-475+STR, National Center for Atmospheric Research, Boulder, CO.
Smagorinsky, J., 1963. General circulation experiments with the primitive equations. Mon. Weather Rev. 91 (3), 99–164.
Strobel, D.F. et al., 1996. On the vertical temperature structure of Pluto's atmosphere. Icarus 120 (2), 266–289.
Toigo, A.D. et al., 2012. The impact of resolution on the dynamics of the martian global atmosphere: Varying resolution studies with the MarsWRF GCM. Icarus 221, 276–288.
Young, E.F. et al., 2008. Vertical structure in Pluto's atmosphere from the 2006 June 12 stellar occultation. Astron. J. 136, 1757–1769.
Young, L.A., 2012. Volatile transport on inhomogeneous surfaces: I – Analytic expressions, with application to Pluto's day. Icarus 221, 80–88.
Young, L.A., 2013. Pluto's seasons: New predictions for New Horizons. Astron. J. 766 (2), L22.
Zalucha, A.M., Gulbis, A.A.S., 2012. Comparison of a simple 2-d Pluto general circulation model with stellar occultation light curves and implications for atmospheric circulation. J. Geophys. Res. 117, E05002. http://dx.doi.org/10.1029/2011JE003957.
Zalucha, A.M., Michaels, T.I., 2013. A 3D general circulation model for Pluto and Triton with fixed volatile abundance and simplified surface forcing. Icarus 223 (2), 819–831.
Zalucha, A.M. et al., 2011a. An analysis of Pluto of occultation light curves using an atmospheric radiative–conductive model. Icarus 211, 804–818.
Zalucha, A.M. et al., 2011b. An investigation of Pluto's troposphere using stellar occultation light curves and an atmospheric radiative–conductive–convective model. Icarus 214, 685–700.
Zangari, A., 2015. A meta-analysis of coordinate systems and bibliography of their use on Pluto from Charon's discovery to the present day. Icarus 246, 93–145.
Zhu, X., Strobel, D.F., Erwin, J.T., 2014. The density and thermal structure of Pluto's atmosphere and associated escape processes and rates. Icarus 228, 301–314.